Green Carbon 1 (2023) 160–169

Contents lists available at ScienceDirect

Green Carbon

journal homepage: www.keaipublishing.com/en/journals/green-carbon/

Research Article

ZIF-8-derived Fe-C catalysts: Relationship between structure and catalytic activity toward the oxygen reduction reaction

Jakub P. Masnica[1], Syed Sibt-e-Hassan[1], Sanja Potgieter-Vermaak[2], Yagya N. Regmi[3], Laurie A. King[4], Lubomira Tosheva[*,5]

Faculty of Science and Engineering, Manchester Metropolitan University, Chester Street, M1 5GD, United Kingdom

ARTICLE INFO

Keywords:
ZIF-8
Self-sacrificial template
Fe-N-C electrocatalysts
Oxygen reduction reaction

ABSTRACT

The oxygen reduction reaction (ORR) activity of carbonized ZIF-8 (CZ) and its Fe-doped derivatives, CZ-A (doped with ammonium iron (II) sulphate) and CZ-B (doped with iron (II) acetate), were examined in both acidic (0.5 M H_2SO_4) and basic (0.1 M KOH) electrolytes using a rotating disk electrode setup. These data show that the ORR activity of the Fe-doped catalysts is higher than that of pure CZ, with a higher activity in basic than acidic electrolyte. Extensive materials characterization highlights important differences in the sample crystallinity, morphology, porosity, and chemical composition as a function of the deployed precursor. The performance of the prepared catalysts is also impacted by the Fe precursor selection, highlighting the importance of such synthetic parameters in controlling the density and identify of Fe-Nx active sites. These results demonstrate the potential application of Fe-doped carbonized ZIF-8 catalysts for the ORR in basic electrolyte and offer important knowledge for the future design of non-precious metal fuel cell electrocatalysts.

1. Introduction

Increasing energy demand and climate change challenges have prompted global action to shift the reliance on fossil fuels to sustainable low carbon technologies. Polymer electrolyte membrane fuel cells (PEMFCs) have been considered as promising energy conversion technologies for transportation and portable device applications with zero emission, high charge density and low operation temperatures [1]. However, despite the significant reduction in system cost and Pt electrocatalyst loading over the past 20 years [2], further advances are important to widen worldwide implementation of both proton exchange (acidic) and anion exchange (alkaline) PEMFCs. The development of platinum group metal (PMG)-free catalysts for the sluggish oxygen reduction reaction (ORR) is urgently needed to address the cost and sustainability of PEMFC production. In recent years, intense research has been focused on the development of Fe-N-C materials as PMG-free alternative ORR catalysts [3–5]. Owing to their permanent porosity, very high surface areas, presence of organic ligands, which can serve as a carbon and heteroatom (such as N and S) source, metal-organic frameworks (MOF) have emerged as promising precursors to ORR PMG-free catalysts [6,7]. Zeolitic imidazole framework-8 (ZIF-8), a MOF material composed of Zn ions and imidazolate linkers, has received special attention by virtue of its remarkable chemical stability, well-established and facile synthesis methods, high N content and Zn mobility during pyrolysis [8–10]. Additionally, Fe-ZIF-8 derived materials have been deployed as ORR catalysts in both acidic and alkaline environments demonstrating their utility in both proton exchange and anion exchange PEMFCs [11].

The morphology, composition, structural characteristics and corresponding ORR activity and stability of Fe-N-C catalysts derived from ZIF-8 depend on many factors such as ZIF-8 synthesis conditions, Fe source and concentration, strategy used for Fe doping, presence of guest molecules, pyrolysis conditions, post-pyrolysis acid leaching, etc. Two approaches for the Fe doping have been investigated; in-situ doping via

* Corresponding author.
E-mail address: l.tosheva@mmu.ac.uk (L. Tosheva).
[1] These authors contributed equally to this work.
[2] ORCID: 0000-0002-1994-7750
[3] ORCID: 0000-0001-6588-7683
[4] ORCID: 0000-0002-0772-2378
[5] ORCID: 0000-0002-3605-9851

https://doi.org/10.1016/j.greenca.2023.11.001
Received 24 July 2023; Received in revised form 20 October 2023; Accepted 7 November 2023
Available online 10 November 2023

a one-pot synthesis, and ex-situ doping by post-synthetic treatments. One-pot synthesis is commonly achieved through the addition of an Fe salt during the preparation of the ZIF-8 precursor solution, most often using methanol as a solvent and at room temperature. Post-synthetic doping, in which pre-prepared ZIF-8 powder is treated with a Fe salt, has also been explored. In the former method, iron compounds such as iron (III) acetylacetonate ($Fe(acac)_3$), $FeCl_3$ and $Fe(NO_3)_3$ [12], $Fe(NO_3)_3{\cdot}9H_2O$ [13], ferrocene [14], and Fe_3O_4 [15] have been added to the ZIF-8 synthesis solution to prepare Fe-ZIF-8, which is then pyrolyzed. In more complex one-pot syntheses, additives have been added together with the Fe salts to the ZIF-8 precursor solution. For example, surfactants such as cetyltrimethylammonium bromide have been added to ZIF-8 precursor solution containing aqueous $Fe(NO_3)_3{\cdot}9H_2O$ to control the crystal morphology and prevent Fe agglomeration during pyrolysis [16]. Two different surfactants, Span 80 and Tween 80, have been added to a one-pot synthesis in an aqueous medium employing $FeSO_4$ to control the ZIF-8 crystal size and crystal size distribution and to prevent the formation of unwanted phases [17]. Carbon black has been added together with $FeCl_3{\cdot}6H_2O$ to promote the formation of graphene-like layered structures and to suppress nanoparticle formation [18]. $FeSO_4{\cdot}7H_2O$ and sodium acetate anhydrous (OAc) have been used, with the OAc enhancing the Fe concentration in the catalysts and improving the mass-transfer through hierarchical porosity [19]. Polystyrene (PS) doped with $Fe(NO_3)_3{\cdot}9H_2O$ has also been used and the PS template was dissolved in tetrahydrofuran prior to pyrolysis to obtain hierarchically ordered porous carbon [20]. Vitamin C and $Fe(acac)_3$ have been added to the ZIF-8 precursor solution prepared in an aqueous medium to control the morphology, structure and composition of the Fe-N-C catalysts obtained [21]. Chen et al. have prepared Fe-ZIF-8 by a one-pot synthesis using $Fe(acac)_3$, which was then followed by the addition of melamine prior to pyrolysis to further increase the ORR activity [22]. Jafari et al. have added iron (III) 2,4-pentanedionate during ZIF-8 synthesis and mixed the obtained powder with pyrrole monomers and $FeCl_3{\cdot}6H_2O$ aqueous solution to prepare iron-based nanoparticles encapsulated in carbon nanotubes (CNTs) [23].

Post-synthetic doping of ZIF-8 with Fe has also been investigated for the preparation of ORR electrocatalysts. For example, hierarchical porous N-doped carbon with Fe/Fe_3C nanoparticles has been prepared by mixing ZIF-8 with potassium ferricyanide in water [24]. N-doped carbon containing Fe_3C nanoparticles and CNTs has been obtained from ZIF-8, iron (II) oxalate and dicyandiamide [25]. ZIF-8 has been treated with $FeCl_3{\cdot}6H_2O$ followed by the addition of polyvinylpyrrolidone to prepare a pyrolyzed dual atom Zn/Fe-NC ORR catalysts [26]. Ferrous sulphate has been mixed with ZIF-8 in the presence of hydrated hydrazine for the synthesis of Fe-N-S co-doped carbon matrix/nanotube nanocomposites [27]. Song et al. used a tetraphenylporphyrin iron polymer, ZIF-8 and anhydrous $FeCl_3$ to form Fe_3O_4 nanoparticles with oxygen vacancies upon pyrolysis [28]. Ballmilling has also been used to prepare Fe-N-C ORR electrocatalysts employing ZIF-8 and 5, 10, 15, 20-Tetrakis (4- methoxyphenyl) - 21H, 23H-porphin iron (III) chloride [29], ZIF-8 and another MOF as a Fe-source, namely MIL-100 (Fe) [30], and a dried slurry made of ZIF-8, 1,10-phenanthroline and ferrous acetate [10]. Fe has also been introduced to pre-carbonized ZIF-8 mixed with $FeCl_3{\cdot}6H_2O$ followed by a second pyrolysis step [31].

The effect of the pyrolysis temperature has been studied in many works [10,13,18,20,23,24,27−29], and generally, pyrolysis temperatures of 900 –1000 °C have been found optimal. However, the direct comparison between such studies is not always possible because of the different pyrolysis atmospheres used, most often N_2 or Ar, but also H_2/Ar (10%:90%) [12,14] or NH_3/Ar (10%:90%) [18]. Finally, the pyrolyzed material is sometimes washed with an acid to remove unstable Fe phases, although changes in the material's characteristics before and after acid leaching are usually not discussed. Acids such as 1 M HNO_3 [12], 0.5 M H_2SO_4 [14,16,19], and 1 M HCl [15] have been used.

Amongst the different synthetic strategies used, one-pot synthesis methods, in which Fe salt is added to the ZIF-8 precursor solution without any additives, are generally preferred. This approach reduces the number of synthesis steps involved, avoiding the repeated use of purification procedures, while also reducing the quantity of solvents required and thus enhancing the potential for upscaling. Further, systematic studies of the influence of the Fe source used for doping within a single study employing the same synthesis conditions otherwise, are rarely performed [12]. Indeed, drawing conclusions about the influence of the Fe salt used for doping based on different works is difficult because of variations in the ZIF-8 synthesis conditions and Fe salt concentrations. $Fe(acac)_3$ and ferrocene have been suggested as the most advantageous dopant sources preferentially forming single-atom Fe-Nx active sites due to the large molecular size of these Fe precursor molecules and restricted encapsulation within the microporous ZIF-8, which is thought to prevent aggregation during pyrolysis [12,14,22]. This, however, restricts the variations in the Fe doping of Fe-N-C catalysts when bulky Fe salts such as $Fe(acac)_3$ and ferrocene were used as Fe sources. For instance, it has been reported that a saturated ferrocene weight ratio of only about 1 wt% can be reached [14]. Furthermore, the divalent Fe^{2+} ion is also preferred as the Fe-doping source because of its similar ionic radius to Zn^{2+} (62 pm compared to 60 pm, respectively) allowing a partial replacement of the Zn ions in ZIF-8, although control measures need to be in place during the synthesis to prevent the oxidation of Fe^{2+} to Fe^{3+} [17].

In this study, different Fe salts were screened as Fe doping salts for ZIF-8 in a one-pot synthesis. Amongst them, two Fe(II) salts, namely ammonium iron (II) sulphate hexahydrate and iron (II) acetate were selected for the preparation of Fe-N-C electrocatalysts to further study the influence of the Fe source on the structure, morphology, and ORR activity. The former compound, which is also a source of S-doping, has not been previously reported for the synthesis of Fe-N-C catalysts. The results reported indicate that higher Fe concentrations could be beneficial for creating hierarchical porosity, which can be tailored by the type of the Fe salt used.

2. Method and materials

2.1. Synthesis of Fe-C materials

Zinc nitrate hexahydrate ($Zn(NO_3)_2{\cdot}6H_2O$, Alfa Aesar), 2-methyl imidazole (Sigma-Aldrich), methanol (Fisher Chemical), ammonium iron (II) sulphate hexahydrate ($(NH_4)_2Fe(SO_4)_2{\cdot}6H_2O$, Thermo Sscientific), iron (II) acetate ($Fe(CO_2CH_3)_2$, Thermo Scientific), ferrocene ($Fe(C_5H_5)_2$, Alfa Aesar), and iron (III) nitrate nonahydrate ($Fe(NO_3)_3{\cdot}9H_2O$, Fisher Scientific) were used as received for the one-pot synthesis of Fe-ZIF-8. In a typical ZIF-8 synthesis, 1.188 g (0.00399 mol) of $Zn(NO_3)_2{\cdot}6H_2O$ were dissolved in 30 ml of methanol in a beaker. In another beaker, 2.628 g (0.023 mol) of 2-methyl immidazole were dissolved in 30 ml of methanol. The two beakers were mixed and stirred at room temperature for 24 h. The ZIF-8 obtained (labelled as Z) was purified by 3 times centrifugation (6000 RPM, 10 min) and redispersion in methanol and dried at 80 °C overnight. The molar ratio of the ZIF-8 synthesis solution was 4 2-methyl immidazole: 0.5 $Zn(NO_3)_2{\cdot}6H_2O$: 185 methanol. For the synthesis of Fe-ZIF-8 doped with ammonium iron (II) sulphate hexahydrate, iron (II) acetate, iron (III) nitrate nonahydrate, and ferrocene, 0.0005 moles were added to the beaker containing the dissolved 2-methylimmidazole prior to mixing with the Zn nitrate solution. The molar ratio of the Fe-ZIF-8 synthesis solution used was 4 2-methyl immidazole: 0.5 $Zn(NO_3)_2{\cdot}6H_2O$: 185 methanol: 0.06 Fe salt. The synthesis (except for ferrocene) was upscaled 3 times and two of the samples prepared, sample Z-A (with ammonium iron (II) sulphate hexahydrate) and sample Z-B (with iron (II) acetate) were prylozed under N_2 atmosphere (900 °C, 3 h, ramp rate of 3 °C min^{-1}) to obtain samples CZ-A and CZ-B, respectively. The ZIF-8 reference

sample (sample Z) was pyrolyzed under the same conditions to give sample CZ.

2.2. Characterization methods

X-ray difftaction (XRD) patterns of ZIF-8, Fe-ZIF-8 and carbonized Fe-ZIF-8 samples were collected using a PANanalytical X'pert Powder X-Ray diffractometer and Cu Kα1 (λ = 1.5406 Å) radiation and a PIXCel 1-D detector. Data was collected in the range 5°–140° 2θ with a step size of 0.013° 2θ and a measuring time of 89 s per step. The samples were rotated at 60 RPM during the data collection. Phase identification was performed using a crystallography open database HighScore Plus Version 4.0. Crystallite sizes were determined using the Size/Strain calculator incorporated into PANalytical Data Viewer with the instrumental broadening function determined using a NIST SRM674b CeO_2 external standard. The morphology of the samples was studied using a Carl Zeiss Crossbeam 350 scanning electrone microscope (SEM). High Angle Annular Dark-Field (HAADF) images were obtained with a scanning transmission electron microscopy (STEM) detector for the CZ-B sample. The STEM sample was prepared on a TEM 400 mesh holey carbon film supported Cu grid (Agar Scientific) using the dry deposition method. The elemental composition of five areas in SEM samples was determined using energy dispersive spectroscopy (EDS) with an EDAX Inc Apollo 40 SDD detector. The samples were pressed into tablets and mounted onto Al stubs prior to EDS analysis. X-ray fluorescence (XRF) data was collected using a Rigaku NEX-CG energy-dispersive X-ray fluorescence spectrometer and an X-ray tube (I_{max} = 2 mA, V_{max} = 50 kV) with a 50 W Pd anode was used for emitting primary radiation. Samples were analyzed as dry solid powders and analysed using Rigaku Profile Fitting-Spectra Quant X (RPF-SQX) Fundamental Parameters program. The nitrogen adsorption isotherm measurements at −196 °C were measured with a Micrometrics ASAP 2020 surface area analyzer. Samples were degassed at 200 °C for 12 h prior to analysis. Surface areas were calculated using the Brunauer–Emmett–Teller (BET) method whilst micropore volumes and external surface areas were determined by the t-plot method. Total pore volumes were calculated from the volume adsorbed at a relative pressure of 0.995. DFT pore size distributions of samples CZ-A and CZ-B were determined using the DFT data software available in Micromeritics ASAP2020. An InVia Renishaw micro-Raman spectrometer fitted with a Peltier-cooled charge-coupled device detector was used to analyze the amorphous carbonaceous character of the synthesized samples. The 514.5 nm line of a continuous wave Ar^+-ion laser was used as excitation source. The instrument was calibrated at the beginning of each set of analysis using a silicon wafer to ensure peak position's accuracy and repeatability. Optimization ensured that the Si peak achieved was at 520.5 cm^{-1} ± 0.05 cm^{-1} with an intensity that was monitored over time. To ensure an acceptable S/N ratio, forty acquisitions of one second each, using a 50x objective, were acquired. A low power was used to ensure that sample decomposition does not occur. Samples were analyzed as received and were mounted on double sided tape fixed onto glass microscope slides in such a way that single particle analysis was facilitated. A minimum of 20 particles per sample were randomly selected and analyzed. X-ray photoelectron spectroscopy (XPS) data was collected on a Kratos Axis Supra system using monochromated Al kα1 radiation (1486.6 eV). Survey scans were collected using a slot collimator with an analysis area of 300 × 700 μm with a pass energy of 160 eV and region scans with a pass energy of 20 or 40 eV. XPS data was analysed using CASA XPS.

2.3. Preparation and drop casting of catalyst inks onto GCD

Prior to catalyst deposition, the glassy carbon disc (GCD) electrode was polished using aqueous alumina suspensions (0.05 μm) on felt polishing pads. This was followed by ultrasonic cleaning of the GCD. To prepare the inks intended for ORR testing on the GCD, a previously reported recipe was followed but with a slight modification [32]. More precisely, 5 mg of each carbonized catalyst was measured and mixed with 50 μL of deionized water. 20 μL of Nafion solution (D-520 dispersion) was added to the mixture, followed by the addition of 450 μL of isoprpyl alcohol (IPA) to achieve a final concentration of 9.615 mg ml^{-1}. Adjustments to the volumes of dispersants were made to maintain a consistent final concentration. The dispersion was bath sonicated for 20 min, followed by three cycles of horn sonication in ice bath (30 s each at 20% amplitude) with a 10 s gap. Finally, the dispersion was bath sonicated for 7 min before 12.3 μL (0.118 mg) of the ink was loaded (drop cast) onto the 5 mm diameter GCD at a rotation rate of 100 RPM with a loading density of 0.6 mg cm^{-2}. Afterwards, the rotation rate was gradually increased to 500 RPM and maintained for 15 min to allow the ink to dry before any electrochemical test.

2.4. Electrochemical testing of ORR activity

The ORR activity was evaluated by performing cyclic voltammetry in both acidic (0.5 M H_2SO_4) and basic (0.1 M KOH) electrolytes purged with either O_2 or N_2 using a three-electrode configuration. The system consisted of an Ag/AgCl/KCl (3 M) reference electrode, a graphite rod counter electrode, and the drop cast GC-RDE with a diameter of 5 mm as the working electrode. For the 0.1 M KOH aqueous solution, the potential sweep range was from 1.0 V to 0.5 V vs. RHE at a scan rate of 10 mV s^{-1}. In the case of the 0.5 M H_2SO_4 aqueous solution, the potential sweep range was from 1.0 V to 0.2 V vs. RHE at the same scan rate. Oxygen purged scans were corrected for background current through the subtraction of a nitrogen sweep. A total of 5 CVs was collected under both O_2 and N_2 purging. Cathodic sweep data plotted from the 4th cycle was collected for each sample. All experiments were performed in triplicate. The representative LSV corresponding to ORR is obtained by selecting the data set closest to the mean values in terms of onset and half-wave potentials. Electrochemical measurements were converted to potential versus the reversible hydrogen electrode (RHE) using the equation:

$$E_{Ag/AgCl} = E_{RHE} - E^{o}_{Ag/AgCl} - 0.059\,pH$$

To access the preliminary stability of the prepared catalysts, CZ, CZ-A and CZ-B were subjected to 500 CV cycles in the oxygen-purged 0.1 M KOH solution at the scan rate of 200 mV s^{-1} and a rotation rate of 1600 RPM. Before and after the 500 CV cycles, the catalysts' nitrogen-corrected LSVs were acquired at a scan rate of 10 mV s^{-1} and rotation rate of 1600 RPM to look for any discernible variations. To probe understanding of the ORR mechanism of the prepared catalysts, nitrogen-corrected LSVs of CZ-A and CZ-B were obtained in 0.1 M KOH at rotation speeds of 1000, 1600, 2200, and 2800 RPM in a potential range of 1.0–0.6 V vs. RHE. Corresponding Koutecký–Levich plots were generated to estimate the number of electrons transferred in the ORR.

3. Results and discussion

3.1. Synthesis of Fe-ZIF-8 materials

To investigate the role of Fe salt identity and oxidation state on Fe-N-C catalysts, four different Fe containing precursors were selected. Specifically, iron (II) acetate, iron (III) nitrate, ferrocene, and ammonium iron (II) sulphate hexahydrate were investigated. Initial experiments to screen different Fe salts in the one-pot synthesis of Fe-ZIF-8 were based on a literature protocol [22] substituting the $Fe(acac)_3$ with the same number of moles of ammonium iron (II) sulphate hexahydrate. Analysis using XRD and XRF confirmed that the ZIF-8 structure was not preserved and the Fe content was 12.2 wt% for the dark brown product (Fig. S1). Further experiments were performed using a signficantly reduced quantity of Fe (0.0005 mol compared to 0.002 mol) and a slightly increased methanol volume (60 ml compared to 45 ml), and the

product maintained a ZIF-8 structure, the BET surface area was 1122 m^2 g^{-1}, and the Fe content (by XRF) was 7.53 wt%. For all subsequent experiments, the synthesis was conducted with this reduced molar ratio, but with different Fe salts, namely iron (II) acetate, iron (III) nitrate, and ferrocene (Fe (II)). The synthesis with ferrocene resulted in a material with a preserved ZIF-8 structure but containing only 0.06 wt% Fe (by XRF) in accordance to previous results [14]. Conversely, the Fe content in the samples prepared with ferrous acetate and ferric nitrate was 7.32 wt% and 3.41 wt%, respectively, and the ZIF-8 structure was preserved in the product samples. The higher Fe content of samples doped with Fe (II) containing precursors compared to Fe (III) precursors support previous reports that Fe(II) is preferred for doping compared to Fe(III) [17]. The ferrocene sample was not selected for further studies owing to the low Fe incorporation. The synthesis of the other three samples doped with ammonium iron (II) sulphate hexahydrate, iron (II) acetate, and iron (III) nitrate nonahydrate was repeated using 3 times more of each reagent. Unfortunately, the upscaling did not work for the sample prepared with $Fe(NO_3)_3$•$9H_2O$; a white precipitate was formed together with the brownish material (Fig. S2) suggesting that stirring of the larger volume of the synthesis solution was not homogeneous and resulted in the formation of unwanted phases, for instance Fe (III) hydroxide formed in the presence of traces of water in the methanol solvent [12]. The upscaled samples prepared with ammonium iron (II) sulphate hexahydrate and iron (II) acetate were labeled as samples Z-A and Z-B, respectively, and selected for further investigations.

XRD was conducted to probe the crystallinity of the prepared Z, Z-A, and Z-B materials (Fig. 1a) (XRD pattenrs in the whole 5°–140° 2θ range measured are provided in Fig. S3). All three samples showed the characteristic ZIF-8 peaks [8] without the presence of any additional peaks associated with potential impurity of iron species, indicating Fe was homogeneously distributed and structurally integrated within the ZIF-8 framework. In addition, the peaks of sample Z-A are broadened and of lower intensity indicating smaller crystallite sizes (Table 1).

Fig. 1b shows nitrogen adsorption desorption isotherms of the three samples and corresponding textural characteristics are listed in Table 1. The Fe-ZIF-8 samples have slightly lower surface areas compared to unmodified ZIF-8. Sample Z-A shows exceptionally high external surface area, which is accompanied with a decrease in the micropore volume. The Fe content (from EDX) of sample Z-B was lower compared to sample Z-A, and sample Z-A also contained sulfur from the Fe salt used.

SEM analysis was used to further study the morphology and crystal size of the three samples, and SEM images at two different magnifications are shown in Fig. 2. The ZIF-8 crystals display the typical rhombic dodecahedral ZIF-8 morphology and a size of about 250 nm (Fig. 1a, d). It is clear that the identity of the Fe precursor influenced the ZIF-8 nucleation rates and larger particles were obtained for the Fe-ZIF-8 samples. Whereas the rhombic dodecahedral morphology was largely preserved within the ca. 1.25 μm crystals in sample Z-B (Fig. 1c,f), the crystals observed in sample Z-A (ca. 3 μm) were more rounded and with rough surfaces coated with fine nanoparticles and visible macropores (Fig. 1b, e). In addition, impurities of other phases, which could be Fe phases not detected by XRD analysis, could be seen in sample Z-B and to a lesser extent in sample Z-A (Fig. 1e, f). Indeed, EDX spot analysis indicated a higher Fe content within the impurity crystals; however, owing to the large EDX sampling volume, no quantitative conclusive data could be obtained. The specific morphology of sample Z-A could explain its very high external surface area (Table 1).

The SEM analysis (Fig. 2) indicated that the unmodified ZIF-8 crystals were much smaller compared to the Fe-ZIF-8 crystals. It should be noted that ZIF-8 was prepared via a small-batch (1x) synthesis, whereas the Fe-ZIF-8 samples were prepared using a large-batch (3x) synthesis. A comparison between the morphology of 1x and 3x samples Z-A and Z-B (Figs. S4 and S5, respectively) demonstrates that there is indeed a difference in the crystal sizes depending on the scaling factor. The Fe-ZIF-8 samples prepared in a small-batch were smaller compared to the large-batch synthesis. Differences were observed in the XRD data as well (Fig. S7). The SEM and XRD comparison indicate that whereas the general product characteristics, namely morphology and XRD patterns, are retained upon upscaling of ZIF-8 synthesis, different nucleation rates are observed depending on the overall volume of the ZIF-8 precursor solution.

3.2. Pyrolyzed Fe-ZIF-8 samples

Fig. 3a shows XRD patterns of the Fe-carbon materials obtained by pyrolysis of Z-A and Z-B in an inert atmosphere, named hereafter as CZ-A and CZ-B. The high background signal can be associated with the use of copper radiation to collect the XRD patterns of the Fe-containing samples [33]. The samples were inhomogeneous and contained several iron phases. The Fe_3C peaks were more clearly defined in sample CZ-B and this diffraction plot also shows prominent peaks corresponding to metallic Fe at 45, 51 and 65° 2θ. The crystallites sizes for the Fe

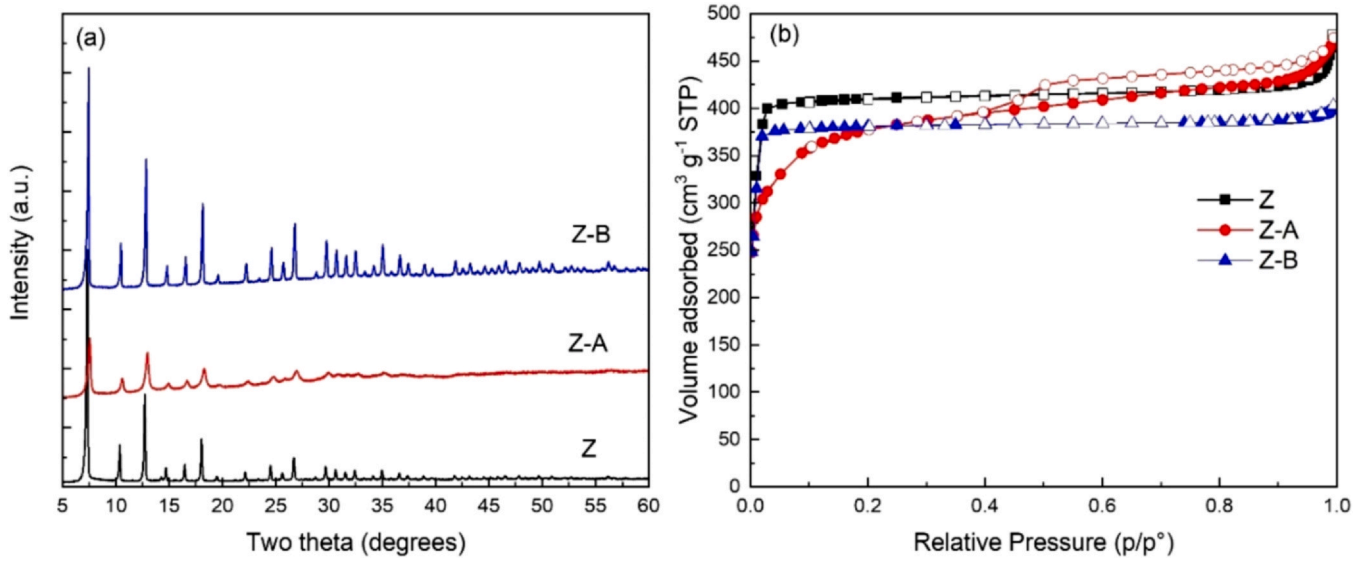

Fig. 1. (a) XRD patterns and (b) nitrogen adsorption desorption isotherms (closed symbols, adsorption; open symbols, desorption) of ZIF-8 (Z) and Fe-ZIF-8 (Z-A and Z-B) samples.

Table 1
Crystallite sizes, Fe and S content*, BET surface areas (S_{BET}), micropore (V_{μ}) and total (V_{TOTAL}) pore volumes and external surface areas (S_{EXT}) of ZIF-8 and Fe-ZIF-8 samples.

Sample	Crystallite size, nm	Fe (at%) ± SD	S (at%) ± SD	S_{BET}, $m^2\ g^{-1}$	V_{μ}, $cm^3\ g^{-1}$	V_{TOTAL}, $cm^3\ g^{-1}$	S_{EXT}, $m^2\ g^{-1}$
Z	60	-	-	1307	0.61	0.74	63
Z-A	20	4.65 ± 0.28	2.40 ± 0.08	1245	0.40	0.73	418
Z-B	50	3.54 ± 0.27	-	1211	0.57	0.62	48

* Determined from EDS.

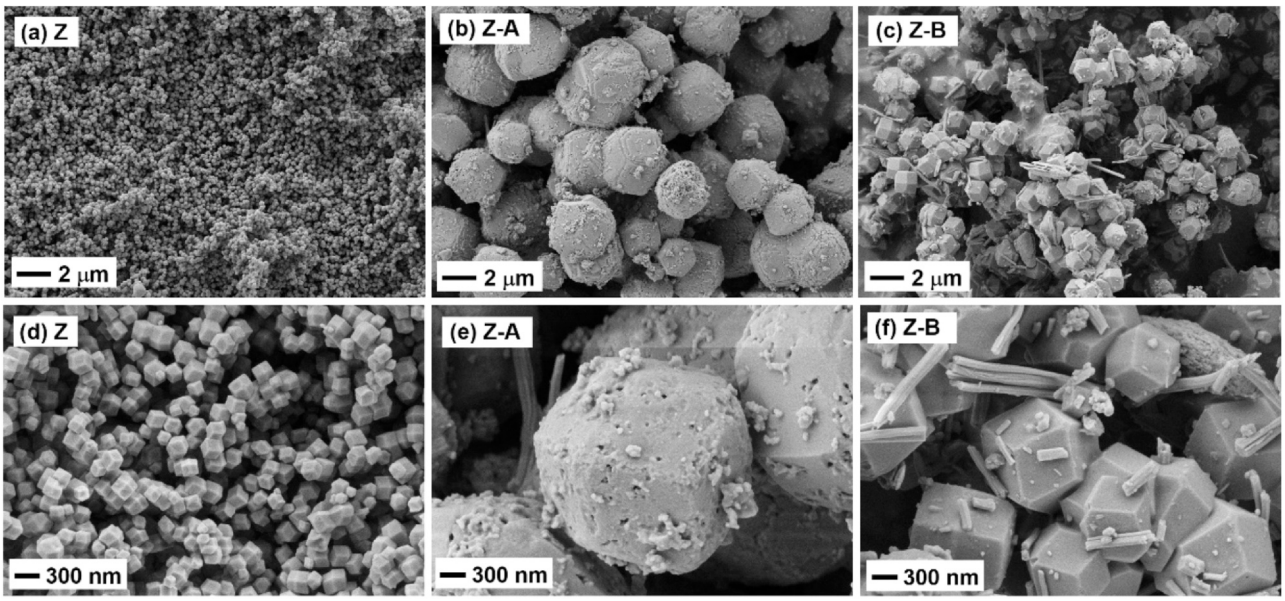

Fig. 2. SEM images at two different magnifications of: (a, d) ZIF-8; (b, e) sample Z-A; and (c, f) sample Z-B.

nanoparticles in CZ-B were determined to be in the 30 nm range. Sample CZ-A showed the presence of FeS_2, which was due to the presence of S in the precursor Z-A sample; Raman analysis further confirmed the presence of iron sulfide phases (Fig. S8). The EDX analysis further indicated that the Zn has either completely evaporated (sample CZ-B) or remained at minimal concentrations (Sample CZ-A) during pyrolysis (Table 2); the latter could probably be related to the larger particle size of CZ-A. In fact, a shiny metal condensed on the inside of the furnace during pyrolysis (Fig. S6), which was confirmed to be Zn by EDX. Metallic Zn has a boiling point of 907 °C and Zn vapors usually escape the ZIF-8 during carbonization [13,21].

To study the carbonized samples, Raman spectra were deconvoluted using the WIRE® software to obtain the G (graphitic) and D (disordered) information of the carbonaceous content. Peak fitting according to Merlen et al. [34] should be as follows: three Lorentzian functions are to be fitted: graphite band G at ~1580 cm^{-1}, and the defect bands D1 and D2 at ~1360 cm^{-1} and 1620 cm^{-1}, respectively, and two Gaussian bands at ~1500 cm^{-1} and 1180 cm^{-1}, respectively

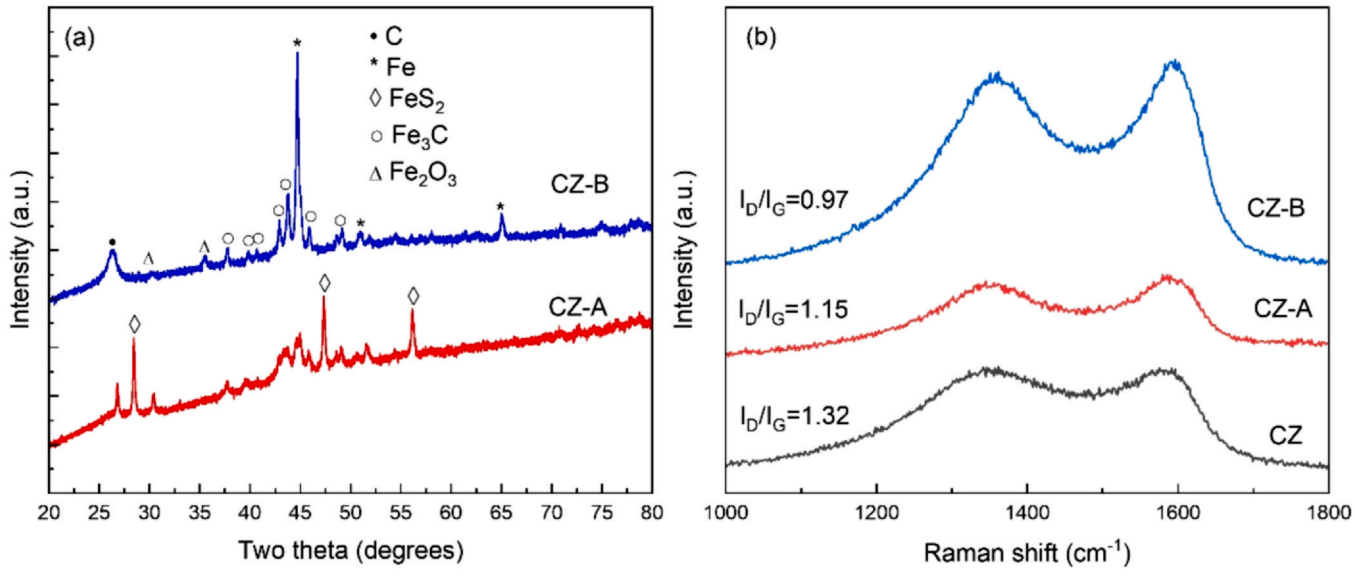

Fig. 3. (a) XRD patterns of samples CZ-A and CZ-B and (b) Raman spectra of pyrolyzed ZIF-8 and Fe-ZIF-8 samples.

Table 2
Fe, S and Zn content*, BET surface areas (S_{BET}), micropore (V_{μ}) and total (V_{TOTAL}) pore volumes and external surface areas (S_{EXT}) of CZ-A and CZ-B samples.

Sample	Fe (at%) ± SD	S (at%) ± SD	Zn (at%) ± SD	S_{BET}, $m^2\ g^{-1}$	V_{μ}, $cm^3\ g^{-1}$	V_{TOTAL}, $cm^3\ g^{-1}$	S_{EXT}, $m^2\ g^{-1}$
CZ-A	9.96 ± 0.28	4.52 ± 0.11	n.d.**	176	0.01	0.16	147
CZ-B	8.89 ± 0.35	-	1.26 ± 0.04	352	0.09	0.44	171

* Determined from EDS.
** not detected.

for D3 and D4. The best fit with the lowest residual was obtained by deconvoluting into 4 bands, D1, D3, D4 and G + D2, which was located at 1595 cm^{-1} and is common for disordered carbons. The Raman spectra (Fig. 3b) are typical of amorphous carbon and indicate the formation of carbon with a low degree of graphitization and the presence of defects and dislocations [35]. The I_D/I_G ratio is indicative of the graphitic content with a ratio > 1 indicating predominantly disorder. It is clear that the inclusion of Fe into the ZIF-8 matrix increases graphitization in samples CZ-A and CZ-B as expected [30]. However, the higher Fe loading in CZ-A compared to CZ-B (c/f Table 2) did not translate to the lowest ratio as expected. The D3 band (out-of-plane vibrations due to defects mainly from the presence of heteroatoms) and the D4 band (carbon atoms outside the planar graphene network often sp^3 and sp^2-sp^3 carbons) [36] occupy 29.6% in the CZ spectrum but increase to 34.0% and 39.8% for CZ-A and CZ-B, respectively, which is similar to that observed in Ref. [30]. This implies an increase in distortion and inclusion or integration of heteroatoms in the graphitic planes.

Samples CZ-A and CZ-B (post pyrolysis) were further studied by SEM (Fig. 4). Sintering was observed in all three samples compared to the samples prior to pyrolysis (Fig. 2) in agreement with results reported in the literature [13]. The morphology of CZ was similar to the morphology of the Z sample. (Fig. 4a, d). The CZ-A crystals are more rounded compared to Z-A with very rough and denser-looking surfaces coated with higher density of larger nanoparticles (Fig. 4b, e). The most striking differences are observed in the morphology of sample CZ-B, in which the original ZIF-8 crystals are sintered and distorted and embedded within a matrix of CNTs (Fig. 4c, f). Such CNTs in Fe-ZIF-8-derrived carbons have been associated with the presence of metallic Fe clusters acting as catalysts for the formation of CNTs [19,23]. The distinct morphology of sample CZ-B could explain the higher graphitization level measured by Raman spectroscopy.

The nitrogen adsorption desorption isotherms and DFT pore-size distributions of CZ-A and CZ-B are shown in Fig. 5. The Fe and S content (from EDX) and textural characteristics are listed in Table 2. The different morphology of the two prepared Fe-ZIF-8 samples is shown to significantly impact the pore structure of the pyrolyzed samples. Sample CZ-B had higher BET surface area, external area, total pore volume and micropore volume, which could be related to the presence of CNTs within this sample. Sample CZ-A had two times lower surface area and lower porosity, which could be due to the formation of dense Fe phase as identified by XRD (Fig. 3a) and the denser appearance of the crystals (Fig. 4e).

XPS was used to assess the oxidation state of the pyrolyzed samples CZ-A and CZ-B. Specifically, the N 1 s, Fe 2p, C 1 s, O 1 s, and S 2p regions were probed (Fig. 6 and Fig. S9). The N 1 s XPS data were deconvoluted to show various nitrogen species. Critically, we note that the N 1 s region can be readily fit with 4 peaks which each have very similar binding energies across the two samples (Table S1) suggesting the two samples contain the same N-containing functional groups. Multi-peak fitting of N 1 s core levels in FeNC catalyst materials is challenging and remains a topic of controversy in the literature [37]. However, the lowest binding energy peak at ~398.5 eV is commonly assigned to pyridinic nitrogen and the peak at 399.5 eV to nitrogen coordinated iron (the Fe-N_x) [37–40]. The two peaks with higher binding energies (~400.8 eV and ~402.2 eV) have previously been assigned as pyrrolic and N-O nitrogen, respectively [37]. The difference between CZ-A and CZ-B is the relative ratio of these four N 1 s peaks. CZ-A contains a high portion of the higher energy peaks (400.8 eV and 402.2 eV) compared to CZ-B suggesting that this sample contains a higher portion of pyrrolic and N-O bonding compared to Fe-N_x functional group. The C 1 s spectra for CZ-A and CZ-B are very similar to each other, although CZ-A contains a relatively higher proportion of N = C or O = C bonding compared to CZ-B. Fe 2p has a poor-signal-to-noise ratio in CZ-B

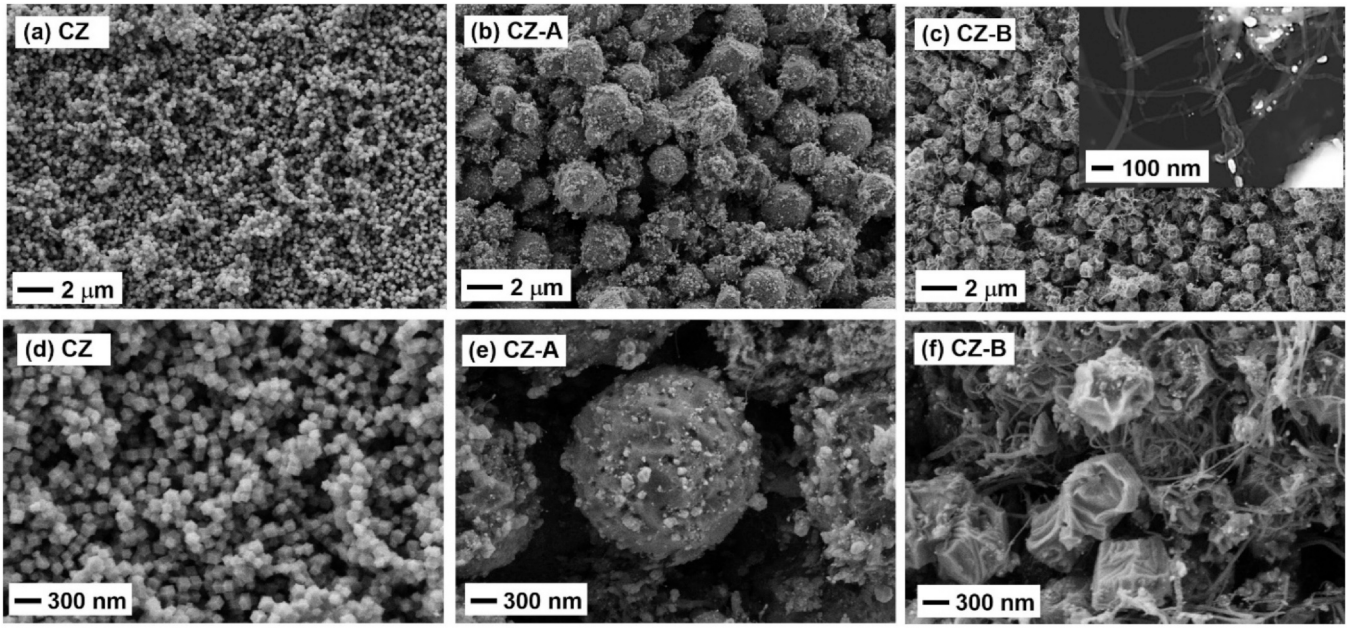

Fig. 4. SEM images at two different magnifications of: (a, d) CZ; (b, e) sample CZ-A; and (c, f) sample CZ-B. The insert in (c) shows an HAADF image of the CNTs formed within this sample.

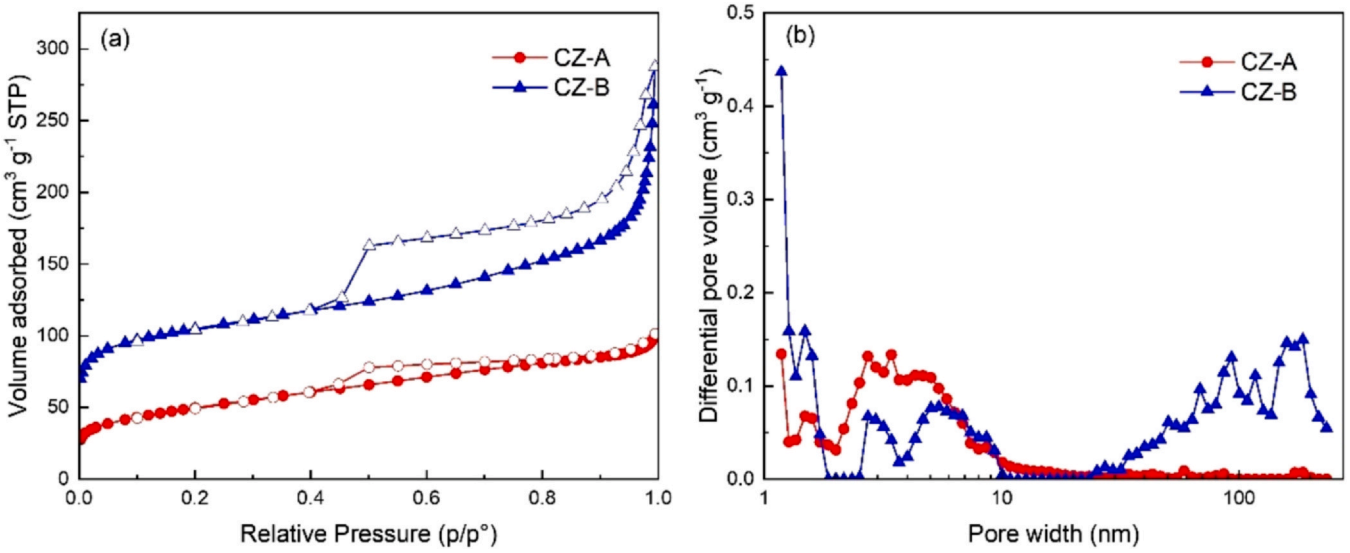

Fig. 5. **(a)** Nitrogen adsorption desorption isotherms (closed symbols, adsorption; open symbols, desorption) of CZ-A and CZ-B, and **(b)** corresponding DFT pore-size distributions.

compared to CZ-A, suggesting potentially a lower Fe incorporation (at the surface of the sample) which suggests a lower surface concentration of Fe in sample CZ-B. This is consistent with the EDX results from samples CZ-A and CZ-B. By XRD, Fe_3C and metallic Fe were observed in CZ-B. The Fe $2p_{3/2}$ region shows two distinct regions at ~707 eV and ~710 eV. The lower binding energies relate to metallic Fe(0) which is consistent with the metallic Fe crystalline peaks observed in CZ-B. This region of lower binding energies could be assigned to FeS_2 which is observed by XRD and Raman in CZ-A. Consistent with previously reported FeNC catalysts, the $2p_{3/2}$ region at ~707 eV is likely a combination of Fe(II) and Fe(III) which are typically observed at ~709.5 eV and ~713.9 eV [41,42]. Finally, as expected based on the starting materials, sample CZ-A (prepared from ammonium iron sulphate) indicates the presence of S whereas no S is present in CZ-B (Fig. S9).

3.3. ORR activity

To examine the ORR activity of the pyrolyzed ZIF, catalysts were drop-cast onto a GCD and assessed using a RDE in both acidic (0.5 M H_2SO_4) and basic (0.1 M KOH) electrolyte (Fig. 7). The electrochemical onset potential, half-wave potential and diffusion limiting current are tabulated for each catalyst (tested in triplicate) in Table 3. For each catalyst assessed, the activity (onset potential, half-wave potential and diffusion limited current) is higher under basic conditions than in acidic. Furthermore, the activity trend of CZ-A > CZ-B > CZ holds in both acidic and alkaline electrolytes. This is despite the significantly higher BET surface area of CZ-B (352 m^2 g^{-1}) compared to the CZ-A (176 m^2 g^{-1}), suggesting that increased surface area alone does not account for these differences in ORR performance. Beyond surface area, post pyrolysis of the ZIF materials, there is a difference in the Fe content between the two samples. Specifically, CZ-B has a lower atomic content (8.89 at% by EDX) in comparison to CZ-A (9.96 at% by EDX) which, as expected for this family of materials, directly impacts the measured catalytic performance.

In acidic electrolyte, the onset potential for CZ was 0.57 V vs. RHE with a standard deviation (SD) of 0.05. The onset potentials for CZ-A and CZ-B were measured to be 0.78 V vs. RHE (SD 0.007) and 0.77 V vs. RHE (SD 0.01), respectively. The corresponding half-wave potentials versus RHE were determined as 0.32 V (SD 0.015) for CZ, 0.7 V (SD 0.028) for CZ-A, and 0.68 V (SD 0.03) for CZ-B. The diffusion limiting

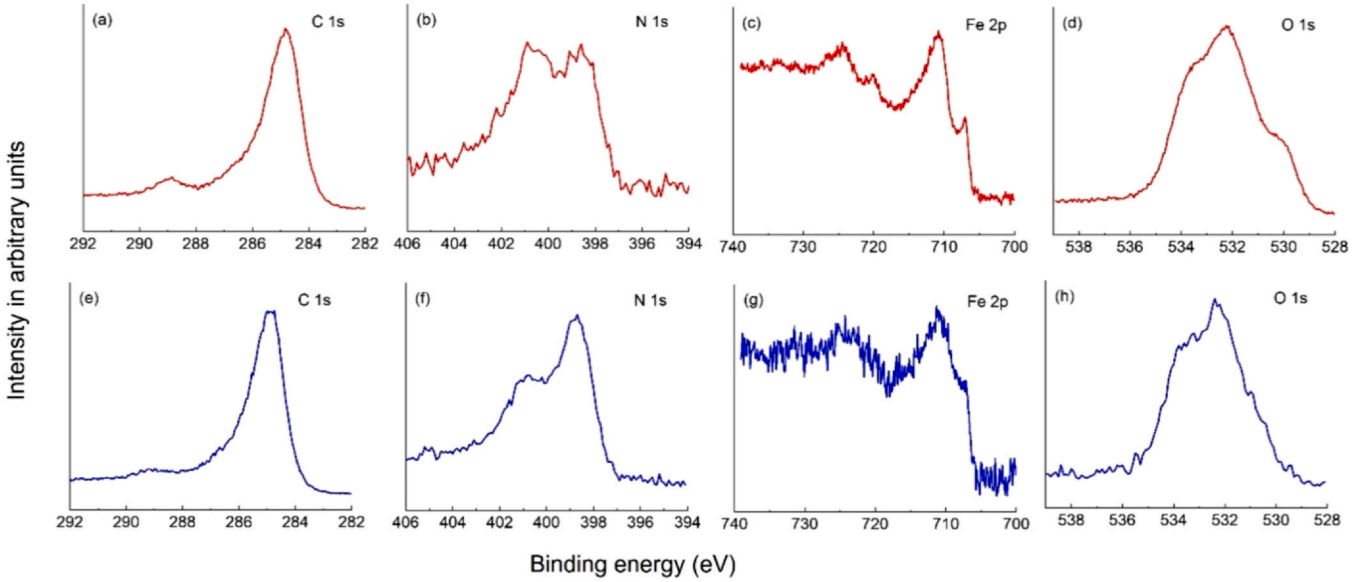

Fig. 6. High resolution C 1 s, N 1 s, Fe 2p and O 1 s XPS spectra of (a,b,c,d) CZ-A and (e,f,g,h) CZ-B.

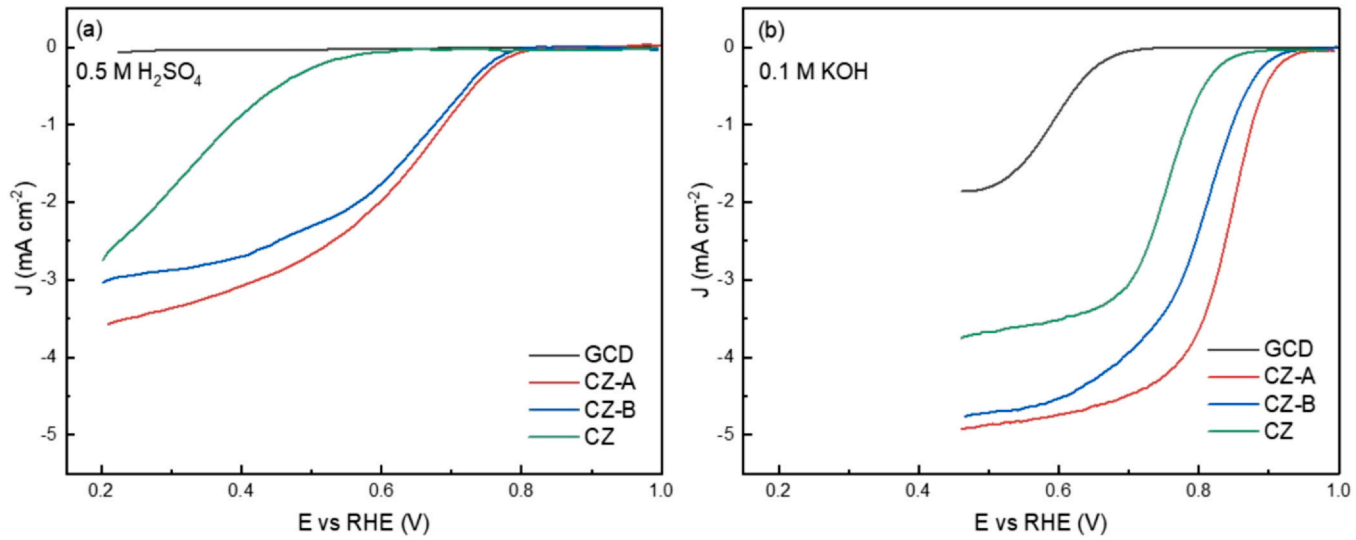

Fig. 7. Electrochemical performance of the pyrolyzed samples (CZ, CZ-A and CZ-B) collected in (a) 0.5 M H_2SO_4 and (b) 0.1 M KOH electrolyte (1600 RPM, O_2 saturated – N_2 saturated current density).

currents, reflecting the mass transport of reactants, were −2.74 mA (SD 0.3) for CZ, −4.57 mA (SD 0.184) for CZ-A, and −3.04 mA (SD 0.04) for CZ-B, suggesting that identity of the Fe salt plays a significant role in controlling the ORR activity of the ZIF-derived catalysts.

Interestingly, in the basic electrolyte, the ORR onset potentials are consistently lower than in acidic environments. Specifically, the onset potential for CZ, CZ-A, and CZ-B were 0.86 V vs RHE (SD 0.064), 0.93 V vs RHE (SD 0.008), and 0.91 V vs RHE (SD 0.012), respectively. The half-wave potentials versus RHE were determined as 0.75 V (SD 0.007) for CZ, 0.85 V (SD 0.008) for CZ-A, and 0.82 V (SD 0.035) for CZ-B. As expected, the electrochemical data demonstrates the enhanced ORR activity of the Fe-doped catalysts, CZ-A and CZ-B, compared to the pure CZ catalyst in both acidic and basic electrolytes. However, it is the results from the basic electrolyte that is particularly noteworthy and promising. More precisely, in terms of the onset and half-wave potentials, as well as the diffusion limiting current, CZ-A and CZ-B exhibit significant improvements over CZ. The ORR activity (onset potential, half-wave potential and diffusion limiting current density) of several literature ZIF-8 derived Fe-N-C catalysts is detailed in Table S2 to enable benchmarking of CZ-A and CZ-B. It is clear that our highest performing catalyst (CZ-A) has a larger onset potential and half-wave potential compared to many literature catalysts suggesting further synthetic refinements are necessary. However, in alkaline electrolyte CZ-A has a relatively high diffusion limiting current density (−4.92 mA cm^{-2}) suggesting that this catalyst has a high selectivity to the four-electron ORR product, water.

These findings highlight the significant influence of Fe doping on the ORR performance of the carbonized ZIF-8 catalysts. Moreover, the choice of Fe source also appears to play a role in determining their structure which directly influences their catalytic performance. To further characterize the electrochemical performance of the prepared catalysts, we conducted preliminary stability measurements and Koutecký-Levich (L-H) analysis in 0.1 M KOH. Promisingly, our catalysts (CZ, CZ-A and CZ-B) showed little degradation under LSV testing after 500 cycles of accelerated CVs (Fig. S10). Moreover, K-L analysis (details provided in the SI) indicates that both CZ-A and CZ-B proceed by a mixture of the 2-electron and 4-electron mechanistic pathway (see Fig. S11). Overall, these findings have important implications for synthetic design when preparing electrocatalysts for oxygen reduction reactions, especially in basic electrolytes. Future studies will optimize the Fe loading for ORR activity as well as quantifying the ORR selectivity using rotating ring disk electrode measurements to further quantify the role of Fe precursor on the Fe-N-C ORR performance.

4. Conclusions

Fe-ZIF-8 materials were studied as precursors for the preparation of Fe-C ORR catalysts upon pyrolysis. Fe (II) precursors were found to be beneficial for the more efficient Fe incorporation in the one-pot synthesis employed. Two Fe-ZIF-8 materials, prepared with ammonium iron (II) sulphate hexahydrate and iron (II) acetate, were upscaled and pyrolyzed to obtain samples CZ-A and CZ-B, respectively. The iron salt precursor was shown to impact the Fe loading, morphology, structure, and textural characteristics of the product. Both samples contained hierarchical porosity, albeit accompanied with a significant reduction in the BET surface area compared to the as-made Fe-ZIF-8 materials, indicating that the Fe source could alone promote the presence of larger pores without the use of additives. Sample CZ-A was found to contain more Fe and lower surface area and pore volume compared to CZ-B. Nevertheless, this sample showed enhanced ORR activity in both alkaline and acidic media compared to CZ-B.

Table 3
Mean values from the electrochemical ORR activity of samples CZ, CZ-A and CZ-B in triplicate. Standard deviations (SD) are also given for each parameter reported.

Catalyst	Onset potential (V) ± SD	Half-wave potential (V) ± SD	Diffusion limiting current density (mA cm^{-2}) ± SD	Electrolyte
CZ	0.57 ± 0.05	0.32 ± 0.015	-2.74 ± 0.3	0.5 M H_2SO_4
CZ-A	0.78 ± 0.007	0.7 ± 0.028	-3.59 ± 0.184	0.5 M H_2SO_4
CZ-B	0.77 ± 0.01	0.68 ± 0.03	-3.04 ± 0.04	0.5 M H_2SO_4
CZ	0.86 ± 0.064	0.75 ± 0.007	-3.76 ± 0.092	0.1 M KOH
CZ-A	0.93 ± 0.008	0.85 ± 0.008	-4.92 ± 0.05	0.1 M KOH
CZ-B	0.91 ± 0.012	0.82 ± 0.035	-4.76 ± 0.007	0.1 M KOH

CRediT authorship contribution statement

Jakub P. Masnica: Methodology, Data curation, Investigation. **Syed Sibt-E-Hassan:** Investigation, Data curation, Writing – review & editing. **Sanja Potgieter-Vermaak:** Investigation, Writing – review & editing. **Yagya N. Regmi:** Supervision, Writing – review & editing. **Laurie A. King:** Supervision, Methodology, Formal analysis, Resources, Writing – review & editing. **Lubomira Tosheva:** Conceptualization, Project administration, Resources, Supervision, Writing – original draft; Writing – review & editing.

Declaration of Competing Interest

Lubomira Tosheva is an associate editor for Green Carbon and was not involved in the editorial review or the decision to publish this article. The authors declare that they have no known competing financial interests or personal relationships that could have appeared to influence the work reported in this paper.

Acknowledgments

Syed Sibt-e-Hassan gratefully acknowledges the support of the Commonwealth Scholarship Commission for providing academic fellowship. The authors wish to thank Dr Gary Miller (MMU) and Dr Hayley Andrews (MMU) for help with sample characterization (XRD, XPS and SEM).

Appendix A. Supporting information

Supplementary data associated with this article can be found in the online version at doi:10.1016/j.greenca.2023.11.001.

References

[1] K. Jiao, J. Xuan, Q. Du, Z. Bao, B. Xie, B. Wang, Y. Zhao, L. Fan, H. Wang, Z. Hou, S. Huo, N.P. Brandon, Y. Yin, M.D. Guiver, Designing the next generation of proton-exchange membrane fuel cells, Nature 595 (2021) 361–369.
[2] B. Pivovar, Catalysts for fuel cell transportation and hydrogen related uses, Nat. Catal. 2 (2019) 562–565.
[3] H.T. Chung, D.A. Cullen, D. Higgins, B.T. Sneed, E.F. Holby, K.L. More, P. Zelenay, Direct atomic-level insight into the active sites of a high-performance PGM-free ORR catalyst, Science 357 (2017) 479–484.
[4] X. Zhang, L. Truong-Phuoc, T. Asset, S. Pronkin, C. Pham-Huu, Are Fe − N − C electrocatalysts an alternative to Pt-based electrocatalysts for the next generation of proton exchange membrane fuel cells? ACS Catal. 12 (2022) 13853–13875.
[5] Y. He, G. Wu, PGM-free oxygen-reduction catalyst development for proton-exchange membrane fuel cells: challenges, solutions, and promises, Acc. Mater. Res. 3 (2022) 224–236.
[6] X. Wen, Q. Zhang, J. Guan, Applications of metal–organic framework-derived materials in fuel cells and metal-air batteries, Coord. Chem. Rev. 409 (2020) 213214.
[7] W. Xiao, M. Cheng, Y. Liu, J. Wang, G. Zhang, Z. Wei, L. Li, L. Du, G. Wang, H. Liu, Functional metal/carbon composites derived from metal − organic frameworks: Insight into structures, properties, performances, and mechanisms, ACS Catal. 13 (2023) 1759–1790.
[8] K.S. Park, Z. Ni, A.P. Côté, J.Y. Choi, R. Huang, F.J. Uribe-Romo, H.K. Chae, M. O'Keeffe, O.M. Yaghi, Exceptional chemical and thermal stability of zeolitic imidazolate frameworks, Proc. Natl. Acad. Sci. USA 103 (2006) 10186–10191.
[9] J. Cravillon, S. Münzer, S.-J. Lohmeier, A. Feldhoff, K. Huber, M. Wiebcke, Rapid room-temperature synthesis and characterization of nanocrystals of a prototypical zeolitic imidazolate framework, Chem. Mater. 21 (2009) 1410–1412.
[10] E. Proietti, F. Jaouen, M. Lefèvre, N. Larouche, J. Tian, J. Herranz, J.-P. Dodelet, Iron-based cathode catalyst with enhanced power density in polymer electrolyte membrane fuel cells, Nat. Commun. 2 (2011) 416.
[11] S. Park, M. Her, H. Shin, W. Hwang, Y.-E. Sung, Maximizing the active site densities of single-atomic Fe − N − C electrocatalysts for high-performance anion membrane fuel cells, ACS Appl. Energy Mater. 4 (2021) 1459–1466.
[12] L. Gao, M. Xiao, Z. Jin, C. Liu, J. Zhu, J. Ge, W. Xing, Correlating Fe source with Fe-N-C active site construction: guidance for rational design of high-performance ORR catalyst, J. Energy Chem. 27 (2018) 1668–1673.
[13] H. Zhang, S. Hwang, M. Wang, Z. Feng, S. Karakalos, L. Luo, Z. Qiao, X. Xie, C. Wang, D. Su, Y. Shao, G. Wu, Single atomic iron catalysts for oxygen reduction in acidic media: particle size control and thermal activation, J. Am. Chem. Soc. 139 (2017) 14143–14149.
[14] J. Wang, G. Han, L. Wang, L. Du, G. Chen, Y. Gao, Y. Ma, C. Du, X. Cheng, P. Zuo, G. Yin, ZIF-8 with ferrocene encapsulated: a promising precursor to single-atom Fe embedded nitrogen-doped carbon as highly efficient catalyst for oxygen electroreduction, Small 14 (2018) 1704282.
[15] J. Ren, Z. Shi, Y. Huang, Zeolitic-imidazolate-framework-derived Fe-NC catalysts towards efficient oxygen reduction reaction, Int. J. Hydrog. Energ. 48 (2023) 12333–12341.
[16] W.-J. Niu, R.-J. Li, W.-W. Zhao, Y.-Y. Yan, E.-P. Feng, J.-L. Chen, B.-N. Gu, M.-J. Liu, Y.-L. Chueh, Hierarchical porous Fe-N/C@surfactant composites synthesized by a surfactant-assisted strategy as high-performance bifunctional oxygen electrodes for rechargeable zinc-air batteries, J. Colloid Interface Sci. 649 (2023) 435–444.
[17] X. Wang, H. Zhang, H. Lin, S. Gupta, C. Wang, Z. Tao, H. Fu, T. Wang, J. Zheng, G. Wu, X. Li, Directly converting Fe-doped metal–organic frameworks into highly active and stable Fe-N-Ccatalysts for oxygen reduction in acid, Nano Energy 25 (2016) 110–119.
[18] P.-Y. Zhang, X.-H. Yang, Q.-R. Jiang, P.-X. Cui, Z.-Y. Zhou, S.-H. Sun, Y.-C. Wang, S.-G. Sun, General carbon-supporting strategy to boost the oxygen reduction activity of zeolitic-imidazolate-framework-derived Fe/N/ carbon catalysts in proton exchange membrane fuel cells, Appl. Mater. Interfaces 14 (2022) 30724–30734.
[19] Y. Liu, F. Tu, Z. Zhang, Z. Zhao, P. Guo, L. Shen, Y. Zhang, L. Zhao, G. Shao, Z. Wang, Molecular scissor tailoring hierarchical architecture of ZIF-derived Fe/N/C catalysts for acidic oxygen reduction reaction, Appl. Catal. B 324 (2023) 122209.
[20] M. Qiao, Y. Wang, Q. Wang, G. Hu, X. Mamat, S. Zhang, S. Wang, Hierarchically ordered porous carbon with atomically dispersed FeN_4 for ultraefficient oxygen reduction reaction in proton- exchange membrane fuel cells, Angew. Chem. Int. Ed. 59 (2020) 2688–2694.
[21] W. Zhang, W. Wub, F. Guo, X. Dong, Fe3C nanoclusters integrated with Fe single-atom planted in nitrogen doped carbon derived from truncated hexahedron zeolitic imidazolate framework for the efficient transfer hydrogenation of halogenated, J. Colloid Interface Sci. 640 (2023) 1068–1079.
[22] X. Chen, N. Wang, K. Shen, Y. Xie, Y. Tan, Y. Li, MOF-derived isolated Fe atoms implanted in N-doped 3D hierarchical carbon as an efficient ORR electrocatalyst in both alkaline and acidic media, Appl. Mater. Interfaces 11 (2019) 25976–25985.
[23] M. Jafari, H. Gharibi, M.J. Parnian, M. Nasrollahpour, M. Vafaee, Iron-nanoparticle-loaded nitrogen-doped carbon nanotube/ carbon sheet composites derived from MOF as electrocatalysts for an oxygen reduction reaction, ACS Appl. Nano Mater. 4 (2021) 459–477.
[24] G. Li, J. Zhang, W. Li, K. Fan, C. Xu, 3D interconnected hierarchical porous N-doped carbon constructed by flake-like nanostructure with Fe/Fe3C for efficient oxygen reduction reaction and supercapacitor, Nanoscale 10 (2018) 9252–9260.
[25] P. Zhao, H. Nie, J. Yu, J. Wang, G. Cheng, A facile synthesis of porous N-doped carbon with hybridization of Fe3C nanoparticle-encased CNTs for an advanced oxygen reduction reaction electrocatalyst, Inorg. Chem. Front. 5 (2018) 2546–2553.
[26] C. Fu, X. Qi, L. Zhao, T. Yang, Q. Xue, Z. Zhu, P. Xiong, J. Jiang, X. An, H. Chen, J.S. Chen, A. Cabot, R. Wu, Synergistic cooperation between atomically dispersed Zn and Fe on porous nitrogen-doped carbon for boosting oxygen reduction reaction, Appl. Catal. B 335 (2023) 122885.
[27] H. Jin, H. Zhou, D. He, Z. Wang, Q. Wu, Q. Liang, S. Liu, S. Mu, MOF-derived 3D Fe-N-S co-doped carbon matrix/nanotube nanocomposites with advanced oxygen reduction activity and stability in both acidic and alkaline media, Appl. Catal. B 250 (2019) 143–149.
[28] K. Song, W. Dong, C. Tang, Z. Zou, Y. Wu, Coupling nano-Fe_3O_4 with oxygen vacancies on a hypercrosslinked iron porphyrin-coated ZIF-8 as a high-efficiency oxygen reduction reaction electrocatalyst, Appl. Catal. A 642 (2022) 118712.
[29] L. Yang, N. Larouche, R. Chenitz, G. Zhang, M. Lefèvre, J.-P. Dodelet, Activity, performance, and durability for the reduction of oxygen in PEM fuel cells, of Fe/N/C electrocatalysts obtained from the pyrolysis of metal-organic-framework and iron porphyrin precursors, Electrochim. Acta 159 (2015) 184–197.
[30] H. Wang, F.-X. Yin, N. Liu, R.-H. Kou, X.-B. He, C.-J. Sun, B.-H. Chen, D.-J. Liu, H.-Q. Yin, Engineering Fe–Fe3C@Fe–N–C active sites and hybrid structures from dual metal–organic frameworks for oxygen reduction reaction in H_2–O_2 fuel cell and Li–O_2 battery, Adv. Funct. Mater. 29 (2019) 1901531.
[31] S. Liu, Q. Meyer, Y. Li, T. Zhao, Z. Su, K. Ching, C. Zhao, Fe–N–C/Fe nanoparticle composite catalysts for the oxygen reduction reaction in proton exchange membrane fuel cells, Chem. Commun. 58 (2022) 2323–2326.
[32] M.S. Ferrandon, I.H. Park, X. Wang, E. Coleman, A.I. Kropf, D. Myers, Enhancing the activity of Fe-NC oxygen reduction reaction electrocatalysts by high-throughput exploration of synthesis parameters, Electrochim. Acta 441 (2023) 141850.
[33] Y.M. Mos, A.C. Vermeulen, C.J.N. Buisman, J. Weijm, X-ray diffraction of iron containing samples: the importance of a suitable configuration, Geomicrobiol. J. 35 (2018) 511–517.
[34] A. Merlen, J.G. Buijnsters, C. Pardanaud, A guide to and review of the use of multiwavelength Raman spectroscopy for characterizing defective aromatic carbon solids: from graphene to amorphous carbons, Coatings 7 (2017) 153.
[35] A. Sadezky, H. Muckenhuber, H. Grothe, R. Niessner, U. Pöschl, Raman microspectroscopy of soot and related carbonaceous materials: spectral analysis and structural information, Carbon 43 (2005) 1731–1742.
[36] I. Martinaiou, A.H.A. Monteverde Videla, N. Weidler, M. Kübler, W.D.Z. Wallace, S. Paul, S. Wagner, A. Shahraei, R.W. Stark, S. Specchia, U.I. Kramm, Activity and degradation study of an Fe-N-C catalyst for ORR in direct methanol fuel cell (DMFC), Appl. Catal. B 262 (2020) 118217.
[37] M. Primbs, Y. Sun, A. Roy, D. Malko, A. Mehmood, M.-T. Sougrati, P.-Y. Blanchard, G. Granozzi, T. Kosmala, G. Daniel, P. Atanassov, J. Sharman, C. Durante, A. Kucernak, D. Jones, F. Jaouen, P. Strasser, Establishing reactivity descriptors for platinum group metal (PGM)-free Fe–N–C catalysts for PEM fuel cells, Energy Environ. Sci. 13 (2020) 2480–2500.
[38] I. Matanovic, K. Artyushkova, P. Atanassov, Understanding PGM-free catalysts by linking density functional theory calculations and structural analysis: perspectives and challenges, Curr. Opin. Electrochem. 9 (2018) 137–144.

[39] Y.-P. Ku, K. Ehelebe, A. Hutzler, M. Bierling, T. Böhm, A. Zitolo, M. Vorokhta, N. Bibent, F.D. Speck, D. Seeberger, I. Khalakhan, K.J.J. Mayrhofer, S. Thiele, F. Jaouen, S. Cherevko, Oxygen reduction reaction in alkaline media causes iron leaching from Fe−N−C electrocatalysts, J. Am. Chem. Soc. 144 (2022) 9753–9763.
[40] D. Singh, K. Mamtani, C.R. Bruening, J.T. Miller, U.S. Ozkan, Use of H_2S to probe the active sites in FeNC catalysts for the oxygen reduction reaction (ORR) in acidic media, ACS Catal. 4 (2014) 3454–3462.
[41] T. Marshall-Roth, N.J. Libretto, A.T. Wrobel, K.J. Anderton, M.L. Pegis, N.D. Ricke, T.Van Voorhis, J.T. Miller, Y. Surendranath, A pyridinic Fe-N4 macrocycle models the active sites in Fe/N-doped carbon electrocatalysts, Nat. Commun. 11 (2020) 5283.
[42] Z. Zhang, J. Sun, F. Wang, L. Dai, Efficient oxygen reduction reaction (ORR) catalysts based on single iron atoms dispersed on a hierarchically structured porous carbon framework, Angew. Chem. Int. Ed. 57 (2018) 9038–9043.